

Influence of magnification threshold on pixel lensing optical depth, event rate and time scale distributions towards M31

F. De Paolis¹, G. Ingresso¹, A.A. Nucita¹, A.F. Zakharov^{2,3}

¹ Dipartimento di Fisica, Università di Lecce and INFN, Sezione di Lecce, CP 193, I-73100, Italy

² Institute of Theoretical and Experimental Physics, 25, B.Chermushkinskaya st., Moscow, 117259, Russia

³ Astro Space Centre of Lebedev Physics Institute, Moscow

Abstract. Pixel lensing is the gravitational microlensing of light from unresolved stars contributing to the luminosity flux collected by a single pixel. A star must be sufficiently magnified, that is, the lens impact parameter must be less than a threshold value u_T if the excess photon flux in a pixel is to be detected over the background. Assuming the parameters of the Isaac Newton Telescope and typical observing conditions, we present maps in the sky plane towards M31 of threshold impact parameter, optical depth, event number and event time scale, analyzing in particular how these quantities depend on u_T in pixel lensing searches. We use an analytical approach consisting of averaging on u_T and the star column density the optical depth, microlensing rate and event duration time scale. An overall decrease in the expected optical depth and event number with respect to the classical microlensing results is found, particularly towards the high luminosity M31 inner regions. As expected, pixel lensing events towards the inner region of M31 are mostly due to self-lensing, while in the outer region dark events dominate even for a 20% MACHO halo fraction. We also find a far-disk/near-disk asymmetry in the expected event number, smaller than that found by Kerins (2004). Both for self and dark lensing events, the pixel lensing time scale we obtain is $\simeq 1 - 7$ days, dark events lasting roughly twice as long as self-lensing events. The shortest events are found to occur towards the M31 South Semisphere. We also note that the pixel lensing results depend on $\langle u_T \rangle$ and $\langle u_T^2 \rangle$ values and ultimately on the observing conditions and telescope capabilities.

Key words. Gravitational lensing; Galaxy: halo; Cosmology: dark matter; Galaxies: individuals: M31; Methods: observational

1. Introduction

Pixel lensing surveys towards M31 (Crotts, 1992; Baillon et al., 1993) can give valuable information to probe the nature of MACHOs (Massive Astrophysical Compact Halo Objects) discovered in microlensing experiments towards the LMC and SMC (Large and Small Magellanic Clouds) (Alcock et al., 1993; Aubourg et al., 1993) and also address the question of the fraction of halo dark matter in the form of MACHOs in spiral galaxies (Alcock et al., 2000).

This may be possible due to both the increase in the number of expected events and because the M31 disk is highly inclined with respect to the line of sight and so microlensing by MACHOs distributed in a roughly spherical M31 halo give rise to an unambiguous signature: an excess of events on the far side of the M31 disk relative to the near side (Crotts, 1992).

Moreover, M31 surveys probe the MACHO distribution in a different direction to the LMC and SMC and observations are made from the North Earth hemisphere, probing the entire halo extension.

The Pixel lensing technique studies the gravitational microlensing of unresolved stars (Ansari et al., 1997). In a dense field of stars, many of them contribute to each pixel. However, if one unresolved star is sufficiently magnified, the increase of the total flux will be large enough to be detected. Therefore, instead of monitoring individual stars as in classical microlensing, one follows the luminosity intensity of each pixel in the image. When a significative (above the background and the pixel noise) photon number excess repeatedly occurs, it is attributed to an ongoing microlensing event if the pixel luminosity curve follows (as a function of time) a Paczynski like curve (Paczynski, 1996).

Clearly, variable stars could mimic a microlensing curve. These events can be recognized by performing observations in several spectral bands and monitoring the

signal from the same pixel for several observing seasons to identify the source.

Two collaborations, MEGA (preceded by the VATT/Columbia survey) and AGAPE have produced a number of microlensing event candidates, which show a rise in pixel luminosity in M31 ((Crotts & Tomaney, 1996; Ansari et al., 1999; Auriere et al., 2001; Calchi Novati et al., 2002)).

More recently, based on observations with the Isaac Newton Telescope on La Palma (Kerins et al., 2001), the MEGA (de Jong et al., 2004), POINT-AGAPE (Paulin-Henriksson et al., 2003; Calchi Novati et al., 2003; Uglesich et al., 2004) and WeCAPP (Riffeser et al., 2003) collaborations claimed to find evidence of several microlensing events.

In particular, the MEGA Collaboration (de Jong et al., 2004) presented the first 14 M31 candidate microlensing events, 12 of which are new and 2 that have been reported by the POINT-AGAPE Collaboration (Paulin-Henriksson et al., 2003). The preliminary analysis of the spatial and timescale distribution of the events supports their microlensing nature. In particular the far-disk/near-disk asymmetry, although not highly significant, is suggestive of the presence of an M31 dark halo.

The POINT-AGAPE Collaboration found in total a subset of four short timescale, high signal-to-noise ratio microlensing candidates, one of which is almost certainly due to a stellar lens in the bulge of M31 and the other three candidates can be explained either by stars in M31 and M32, or by MACHOs.

In pixel lensing surveys, although all stars contributing to the same pixel are candidates for a microlensing event, only the brightest stars (usually blue and red giants) will be magnified enough to be detectable above background fluctuations (unless for very high amplification of main sequence stars, which are very unlikely events).

First evaluations have shown that the pixel lensing technique towards M31 may give rise to a significant number of events due to the large number of stars contributing to the same pixel (Baillon et al., 1993; Jetzer, 1994; Gould, 1994; Colley, 1995; Han & Gould, 1996).

Although these analytic estimates may be very rough, they provide useful qualitative insights. To have reliable estimates in true observational conditions one should use Monte-Carlo simulations (Ansari et al., 1997; Kerins et al., 2001). In this way, given the capabilities of the telescope and CCD camera used, the observing campaign and weather conditions, one can estimate the event detection efficiency as a function of event duration and maximum amplification.

This study will be done in a forthcoming paper (De Paolis et al., 2004) with the aim of investigating the lens nature (i.e. the population to which the lens belongs) for the events discovered by MEGA (de Jong et al., 2004) and POINT-AGAPE (Paulin-Henriksson et al., 2003).

In this paper, instead of using Monte-Carlo simulations, we estimate the relevant pixel lensing quantities

by analyzing the effect of the presence of a magnification threshold (or, equivalently, of a threshold impact parameter u_T) in pixel lensing searches towards M31. We use an analytic procedure consisting of averaging the classical optical depth, microlensing rate and event duration time scale on u_T , which depends on the magnitude of the source being magnified.

The paper is organized as follows. In Section 2 we briefly discuss the source - bulge and disk stars in M31 - and lens - stars in M31 and in the Milky Way (MW) disk, MACHOs in M31 and MW halos - models we use. In Section 3 we discuss the pixel lensing technique. In Sections 4 and 5 we present maps of optical depth, event rate and typical event time duration, addressing the modification with respect to classical microlensing values, due to the influence of the threshold magnification in pixel lensing searches. Finally in Section 6 we present some conclusions.

2. Source and lens models

The M31 disk, bulge and halo mass distributions are described adopting the parameters of the Reference model in Kerins (2004), which provides remarkably good fits to the M31 surface brightness and rotation curve profiles.

This model, by using an average set of parameter values less extreme with respect to the massive halo, massive bulge and massive disk models in Table 1, can be considered a more likely candidate model for the mass distributions in the M31 galaxy.

Accordingly, the mass density of the M31 disk stars is described by a sech-squared profile

$$\rho_D(R, z) = \rho_D(0) \exp(-R/h) \operatorname{sech}^2(z/H), \quad (1)$$

where R is the distance on the M31 disk plane, $H \simeq 0.3$ kpc and $h \simeq 6.4$ kpc are, respectively, the scale height and scale lengths of the disk and $\rho_D(0) \simeq 3.5 \times 10^8 M_\odot \text{ kpc}^{-3}$ is the central mass density. The disk is truncated at $R \simeq 40$ kpc so that the total mass is $5.3 \times 10^{10} M_\odot$.

As usual, the M31 disk is assumed to be inclined at the angle $i = 77^\circ$ and the azimuthal angle relative to the near minor axis $\phi = -38.6^\circ$.

The M31 bulge is parameterized by a flattened power law of the form

$$\rho_B(R, z) = \rho_B(0) \left[1 + \left(\frac{R}{a} \right)^2 + q^{-2} \left(\frac{z}{a} \right)^2 \right]^{-s/2}, \quad (2)$$

where the coordinates x and y span the M31 disk plane (z is perpendicular to it), $\rho_B(0) \simeq 4.5 \times 10^9 M_\odot \text{ kpc}^{-3}$, $q \simeq 0.6$ is the ratio of the minor to major axes, $a \simeq 1$ kpc and $s \simeq 3.8$ (Reitzel et al., 1998). The bulge is truncated at 40 kpc and its total mass is $\simeq 4.4 \times 10^{10} M_\odot$.

The dark matter in the M31 halo is assumed to follow an isothermal profile

$$\rho_H(r) = \rho_H(0) \frac{a^2}{a^2 + r^2}, \quad (3)$$

Table 1. Parameters for the four M31 models considered by Kerins (2004). Columns are the model name, the component name, the mass of the component, its central density ρ_0 and the adopted cut-off radius R . Additional columns give, where appropriate, the core radius a , the disk scale length h and height H , the flattening parameter q and the B-band mass-to-light ratio M/L_B in solar units.

Model	Component	Mass ($\times 10^{10} M_\odot$)	ρ_0 ($\times M_\odot \text{ pc}^{-3}$)	R (kpc)	a (kpc)	h (kpc)	H (kpc)	q	M/L_B
Massive halo	halo	191	0.25	155	2	-	-	1	-
	bulge	4.4	4.5	40	1	-	-	0.6	9
	disk	3.2	0.24	40	-	6	0.3	-	4.5
Massive bulge	halo	89	0.01	85	10	-	-	1	-
	bulge	8	2.5	40	1.5	-	-	0.6	14
	disk	11	0.6	40	-	7	0.3	-	18
Massive disk	halo	79	0.01	110	8	-	-	1	-
	bulge	4.4	4.5	40	1	-	-	0.6	9
	disk	19	1.4	40	-	6	0.3	-	26
Reference	halo	123	0.065	100	4	-	-	1	-
	bulge	4.4	4.5	40	1	-	-	0.6	9
	disk	5.3	0.35	40	-	6.4	0.3	-	8

with core radius $a \simeq 4$ kpc, and central dark matter density $\rho_H(0) \simeq 6.5 \times 10^7 M_\odot \text{ kpc}^{-3}$, so that the total rotational velocity in the M31 halo is $v_{rot} \simeq 235 \text{ km s}^{-1}$. The M31 halo is truncated at $R \simeq 100$ kpc and the total dark mass within this distance is $\simeq 1.23 \times 10^{12} M_\odot$.

As usual, the mass density profile for a MW disk is described with a double exponential profile

$$\rho_D(R, z) = \rho_D(R_0) \exp(-(R - R_0)/h) \exp(-|z|/H), \quad (4)$$

with the Earth's position from the Galactic center at $R_0 \simeq 8.5$ kpc, scale height $H \simeq 0.3$ kpc, scale length $h \simeq 3.5$ kpc and local mass density $\rho_D(R_0) \simeq 1.67 \times 10^8 M_\odot \text{ kpc}^{-3}$.

The MW bulge¹ is described by the triaxial bulge model with mass density profile (Dwek et al., 1995)

$$\rho_B(x, y, z) = \frac{M_B}{8\pi abc} e^{-s^2/2}, \quad (5)$$

where $s^4 = [(x/a)^2 + (y/b)^2]^2 + (z/c)^4$, the bulge mass is $M_B \simeq 2 \times 10^{10} M_\odot$ and the scale lengths are $a \simeq 1.49$ kpc, $b \simeq 0.58$ kpc and $c \simeq 0.40$ kpc. Here, the coordinates x and y span the Galactic disk plane, whereas z is perpendicular to it.

The dark halo in our Galaxy is also assumed to follow an isothermal profile with core radius $a \simeq 5.6$ kpc and local dark matter density $\rho_H(R_0) \simeq 1.09 \times 10^7 M_\odot \text{ kpc}^{-3}$. The corresponding total asymptotic rotational velocity is $v_{rot} \simeq 220 \text{ km s}^{-1}$. The MW halo is truncated at $R \simeq 100$ kpc and the dark mass within this distance is $\simeq 1.30 \times 10^{12} M_\odot$.

For both M31 and MW halos, the fraction of dark matter in form of MACHOs is assumed to be $f_{MACHO} \simeq 0.2$ (Alcock et al., 2000).

Moreover, as usual, we assume the random velocities of stars and MACHOs to follow Maxwellian distributions with one-dimensional velocity dispersion $\sigma = 30, 100, 166$

¹ Although it does not contribute to microlensing towards M31, it contributes to the dynamical mass of the Galaxy.

km s^{-1} and $30, 156 \text{ km s}^{-1}$ for the M31 disk, bulge, halo and MW disk and halo, respectively (see also Kerins et al. (2001); An et al. (2004)). In addition an M31 bulge rotational velocity of 30 km s^{-1} is assumed.

3. Pixel lensing basics

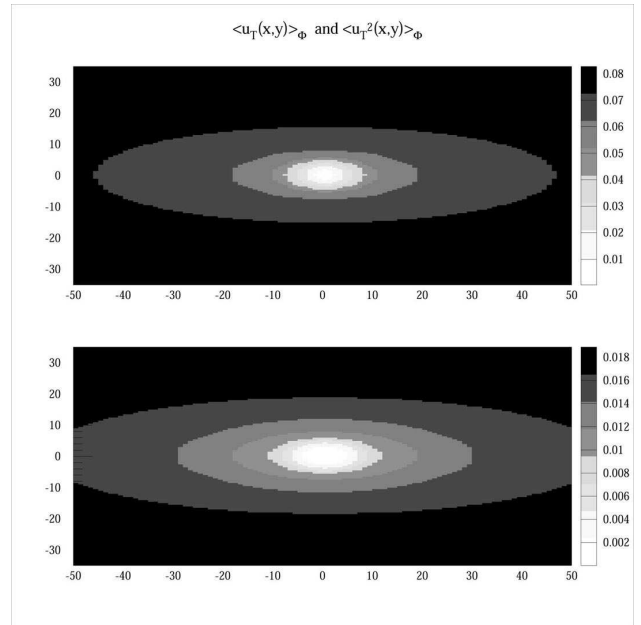


Fig. 1. The mean impact parameter maps $\langle u_T(x, y) \rangle_\phi$ and $\langle u_T^2(x, y) \rangle_\phi$ towards M31 are given, for selected directions towards M31 corresponding to different (x, y) coordinates (in units of arcmin) centered on M31 and aligned along the major and minor axes of the projected light profile.

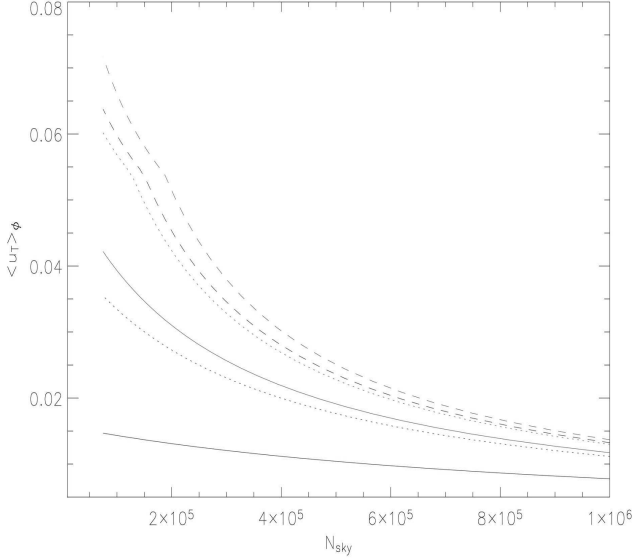


Fig. 2. The mean impact parameter $\langle u_T(x, y) \rangle_\phi$ is given as a function of the background photon counts N_{sky} in a pixel, for selected directions towards M31 corresponding to different (x, y) coordinates (in units of arcmin) in the sky plane. Thin lines, from the bottom to the upper part of the figure, refer to (8, 0), (16, 0) and (32, 0); thick lines are for (0, -2), (0, -4) and (0, -8) coordinates, respectively.

The main difference between gravitational microlensing and pixel lensing observations relies in the fact that in pixel lensing a large number of stars contribute to the same pixel and therefore only bright and sufficiently magnified sources can be identified as microlensing events. In pixel lensing analysis one usually defines a minimum amplification that depends on the baseline photon counts (Ansari et al., 1997)

$$N_{\text{bl}} = N_{\text{gal}} + N_{\text{sky}} , \quad (6)$$

which is the sum of the M31 surface brightness and sky contribution.

The excess photon counts per pixel due to an ongoing microlensing event is

$$\Delta N_{\text{pix}} = N_{\text{bl}}[A_{\text{pix}} - 1] = f_{\text{see}} N_s [A(t) - 1] , \quad (7)$$

where N_s and N_{bl} are the source and baseline photon counts in the absence of lensing, $A(t)$ is the source magnification factor due to lensing and f_{see} is the fraction of the seeing disk contained in a pixel.

As usual, the amplification factor is given by (see, e. g., Griest (1991) and references therein)

$$A(u) = \frac{u^2 + 2}{\sqrt{u^2(u^2 + 4)}} , \quad (8)$$

where

$$u(t)^2 = u_0^2 + \left(\frac{t - t_0}{t_E} \right)^2 \quad (9)$$

is the impact distance in units of the Einstein radius

$$R_E = \left[\frac{4Gm_l}{c^2} D_l (D_s - D_l) / D_s \right]^{1/2} , \quad (10)$$

and u_0 is the impact parameter in units of R_E . Moreover, $t_E = 2R_E/v_\perp$ is the Einstein time, t_0 the time of maximum magnification, D_s and D_l are the source and lens distances from the observer and v_\perp is the lens transverse velocity with respect to the line of sight.

The number of photons in a pixel is given by

$$N_{\text{pix}} = \Delta N_{\text{pix}} + N_{\text{bl}} , \quad (11)$$

and a pixel lensing event will be detectable if the excess pixel photon counts ΔN_{pix} are greater than the pixel noise

$$\sigma = \max(\sigma_T, \sqrt{N_{\text{pix}}}) , \quad (12)$$

σ_T being the minimum noise level determined by the pixel flux stability and $\sqrt{N_{\text{pix}}}$ the statistical photon fluctuation.

By regarding a signal as being statistically significant if it occurs at a level 3σ above the baseline counts N_{bl} , one obtains $A_{\text{min}} \geq 1 + 3\sigma/(f_{\text{see}}N_s)$. If σ is taken equal to the minimum noise level σ_T , the obtained threshold magnification A_T is (Kerins et al., 2001)

$$A_T = 1 + 0.0075 \frac{N_{\text{bl}}}{f_{\text{see}}N_s} \quad (13)$$

which corresponds to a threshold value u_T for the impact distance via the relation in eq. (8). As one can see, u_T depends on the source magnitude M , the line of sight to M31 and the observing conditions.

4. Pixel lensing optical depth and event rate

In pixel lensing analysis, the effect of the existence of the threshold magnification (or, equivalently, of a threshold value of the impact parameter) is usually taken into account in estimating the pixel lensing rate (Kerins et al., 2001, 2003)

$$\Gamma_p(x, y) = \langle u_T(x, y) \rangle_\phi \Gamma_c(x, y) , \quad (14)$$

where x and y are coordinates in the plane orthogonal to the line of sight and $\langle u_T(x, y) \rangle_\phi$ is averaged on the source magnitude M , namely

$$\langle u_T(x, y) \rangle_\phi = \frac{\int_{M_1}^{M_2} u_T(M; x, y) \phi(M) dM}{\int_{M_1}^{M_2} \phi(M) dM} , \quad (15)$$

$M_1 - M_2$ (to be specified below) being the limiting values for the source magnitude and $\phi(M)dM$ the luminosity function, i.e. the number density of sources in the absolute magnitude interval $(M, M + dM)$.

Pixel lensing event detection is usually performed in R or I bands in order to minimize light absorption by the intervening dust in M31 and MW disks. Indeed, these bands offer the best compromise between sampling and sky background, while other bands (B and V) are commonly used to test achromaticity of the candidate events.

In the present analysis, as reference values, we adopt the parameters of the Sloan-r filter on the Wide-Field Camera of the Isaac Newton Telescope (Kerins et al.,

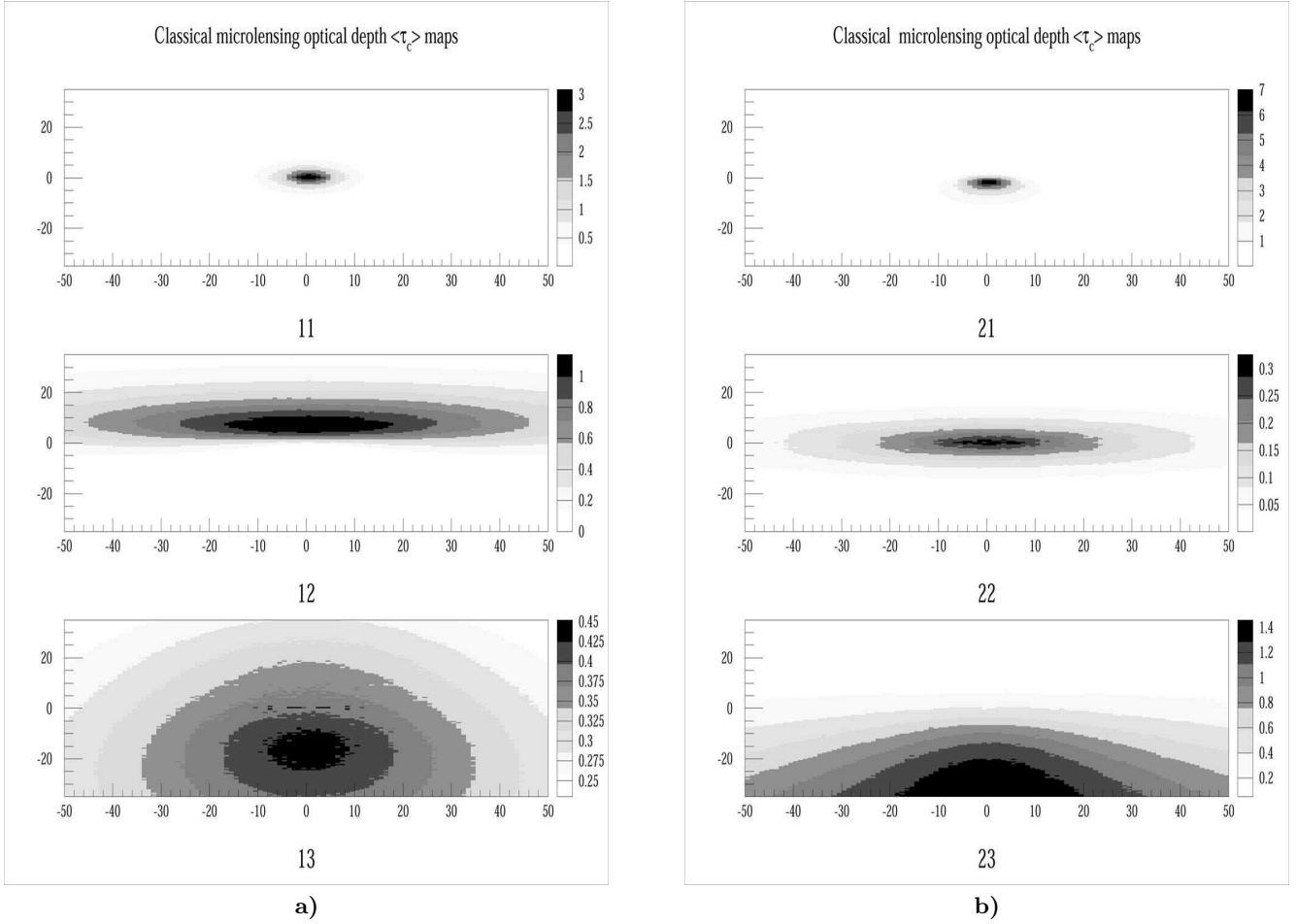


Fig. 3. Mean optical depth $\langle\tau_c(x, y)\rangle$ maps (in units of 10^{-6}) towards M31 are given for selected source and lens populations. The first index refers to the source stars (1 for M31 bulge, 2 for M31 disk) while the second one refers to the lens populations (1 and 2 as above, 3 for MACHOs in the M31 halo). Optical depth maps for lenses belonging to the MW disk and halo populations are not given since the obtained results are almost constant in any direction.

2001). Therefore, since the red giants are the most luminous stars in the red band, we may safely assume that the overwhelming majority of the pixel lensing event sources are red giants. Moreover, gives the lack of precise information about the stellar luminosity function in the M31 galaxy, we assume that the same function $\phi(M)$ holds both for the Galaxy and M31 and does not depend on position.

Accordingly, in the range of magnitude $-6 \leq M \leq 16$ the stellar luminosity function is proportional to the following expression (Mamon & Soneira, 1982)

$$\phi(M) \propto \frac{10^{\beta(M-M^*)}}{[1 + 10^{-(\alpha-\beta)\delta(M-M^*)}]^{1/\delta}}, \quad (16)$$

where, in the red band, $M^* = 1.4$, $\alpha \simeq 0.74$, $\beta = 0.045$ and $\delta = 1/3$.

On the other hand, the fraction of red giants (over the total star number) as a function of M can be approximated as (Mamon & Soneira, 1982)

$$\begin{aligned} f_{RG}(M) &= 1 - C \exp[\alpha(M + \beta)^\gamma] & \text{for } -6 \leq M \leq 3 \\ &= 0 & \text{for } M \geq 3, \end{aligned} \quad (17)$$

where, in the red band, $C \simeq 0.31$, $\alpha \simeq 6.5 \times 10^{-4}$, $\beta = 7.5$ and $\gamma \simeq 3.2$. Therefore, the fraction of red giants averaged over the magnitude is given by

$$\langle f_{RG} \rangle = \frac{\int_{-6}^3 \phi(M) f_{RG}(M) dM}{\int_{-6}^{16} \phi(M) dM}, \quad (18)$$

from which we obtain $\langle f_{RG} \rangle \simeq 5.3 \times 10^{-3}$.

Averaging the pixel lensing rate in eq. (14) on the source density we obtain

$$\langle \Gamma_p(x, y) \rangle = \langle u_T(x, y) \rangle_\phi \langle \Gamma_c(x, y) \rangle_{n_s}, \quad (19)$$

where the mean classical rate $\langle \Gamma_c(x, y) \rangle_{n_s}$ is

$$\langle \Gamma_c(x, y) \rangle_{n_s} = \frac{\int \Gamma_c(D_s; x, y) n_s(D_s; x, y) dD_s}{\int n_s(D_s; x, y) dD_s}. \quad (20)$$

In turn, for a fixed source distance, $\Gamma_c(D_s; x, y)$ is obtained by the classical microlensing rate for a lens of mass m_l (Griest, 1991), by averaging on the lens mass, namely

$$\Gamma_c(D_s; x, y) = \frac{\int \Gamma_c(m_l; D_s, x, y) P(m_l) dm_l}{\int P(m_l) dm_l}, \quad (21)$$

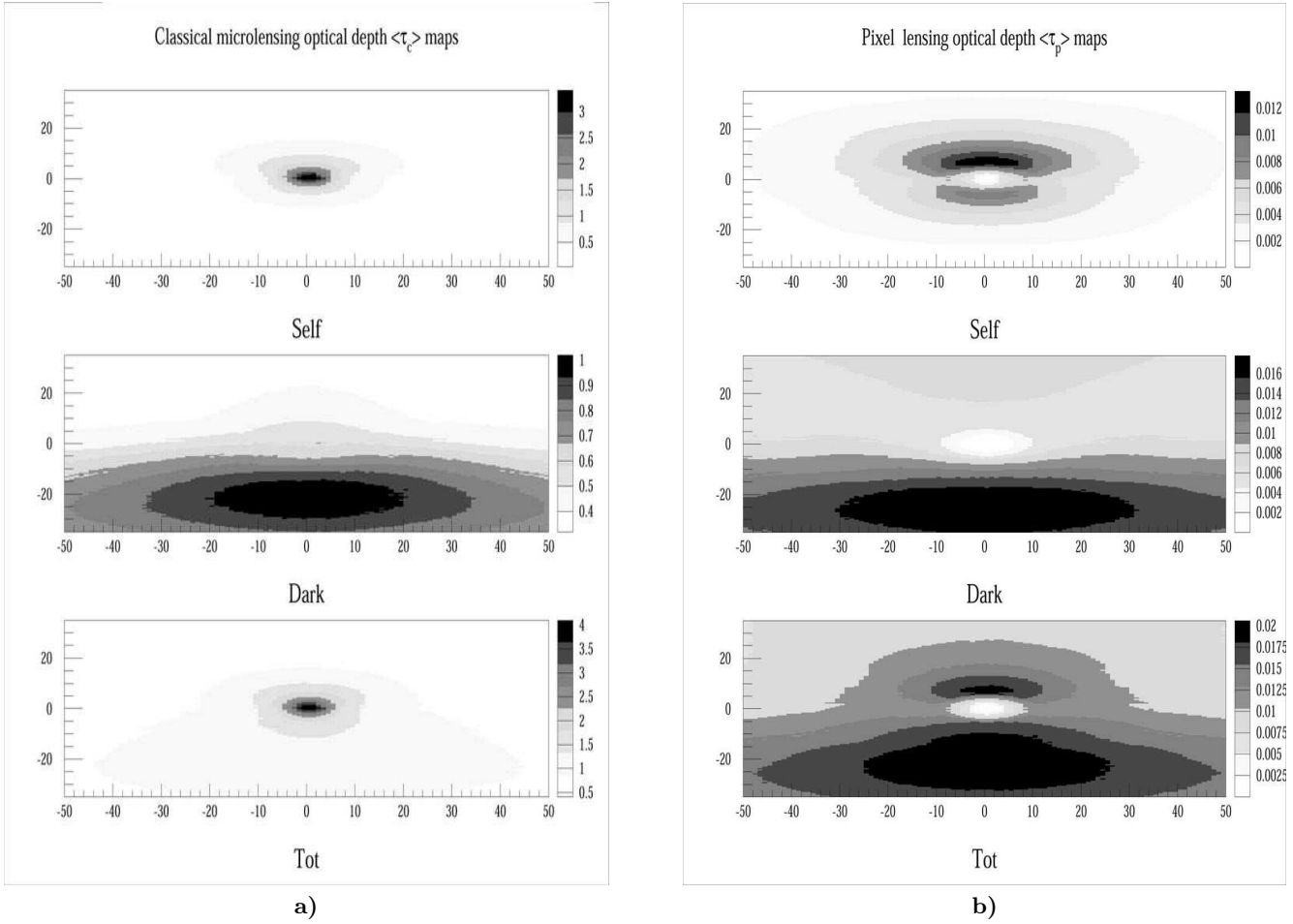


Fig. 4. In panel a), the mean classical optical depth $\langle\tau_c(x, y)\rangle$ maps (in units of 10^{-6}) towards M31 are given for self, dark and total lensing. In panel b), the mean pixel lensing optical depth $\langle\tau_p(x, y)\rangle$ maps are given, in the same cases.

where $P(m_l)$ is the lens mass distribution function.

For lenses belonging to the bulge and disk star populations, lenses are assumed to follow a broken power law (see e.g. An et al. (2004) and references therein)

$$\begin{aligned} P(m_l) &\propto m_l^{-1.4} \quad \text{for } 0.1 M_\odot \leq m_l \leq 0.5 M_\odot \\ &\propto m_l^{-2.2} \quad \text{for } 0.5 M_\odot \leq m_l \leq (m_l)_{up} \end{aligned} \quad (22)$$

where the upper limit $(m_l)_{up}$ is $1 M_\odot$ for M31 bulge stars and $10 M_\odot$ for M31 and MW disk stars. The resulting mean mass for lenses in the bulges and disks are $\langle m_b \rangle \sim 0.31 M_\odot$ and $\langle m_d \rangle \sim 0.53 M_\odot$, respectively.

For the lens mass in the M31 and MW halos we assume the δ -function approximation and we take a MACHO mass $m_{MACHO} \simeq 0.5 M_\odot$, according to the mean value in the analysis of microlensing data towards LMC (Alcock et al., 2000).

As usual, the mean number of expected events in classical microlensing $\langle E_c(x, y) \rangle$ and pixel lensing $\langle E_p(x, y) \rangle$, respectively, are related to the observation time t_{obs} , source column density N_s and mean fraction of red giants $\langle f_{RG} \rangle$ by

$$\langle E_c(x, y) \rangle = \langle \Gamma_c(x, y) \rangle_{n_s} t_{obs} N_s(x, y) \langle f_{RG} \rangle, \quad (23)$$

$$\langle E_p(x, y) \rangle = \langle \Gamma_p(x, y) \rangle_{n_s} t_{obs} N_s(x, y) \langle f_{RG} \rangle, \quad (24)$$

where the source column density is

$$N_s(x, y) = \int n_s(D_s; x, y) dD_s. \quad (25)$$

However, the classical microlensing rate depends on several source and lens parameters, in particular on the lens mass and transverse velocity of the source and lens. Therefore, due to the parameter degeneracy, it does not give precise information on the lens population, at least in the M31 regions where microlensing by stars in M31 itself (self-lensing) and by MACHOs in M31 and MW halos (dark lensing) occur with comparable probability. Indeed, as usual, the probability for a given lens population is

$$P_l = \frac{\sum_s \Gamma_{sl}}{\sum_s \sum_l \Gamma_{sl}}. \quad (26)$$

On the other hand, the classical microlensing optical depth

$$\tau_c(D_s; x, y) = \int_0^{D_s} \pi R_E^2 n_l(D_l) dD_l \quad (27)$$

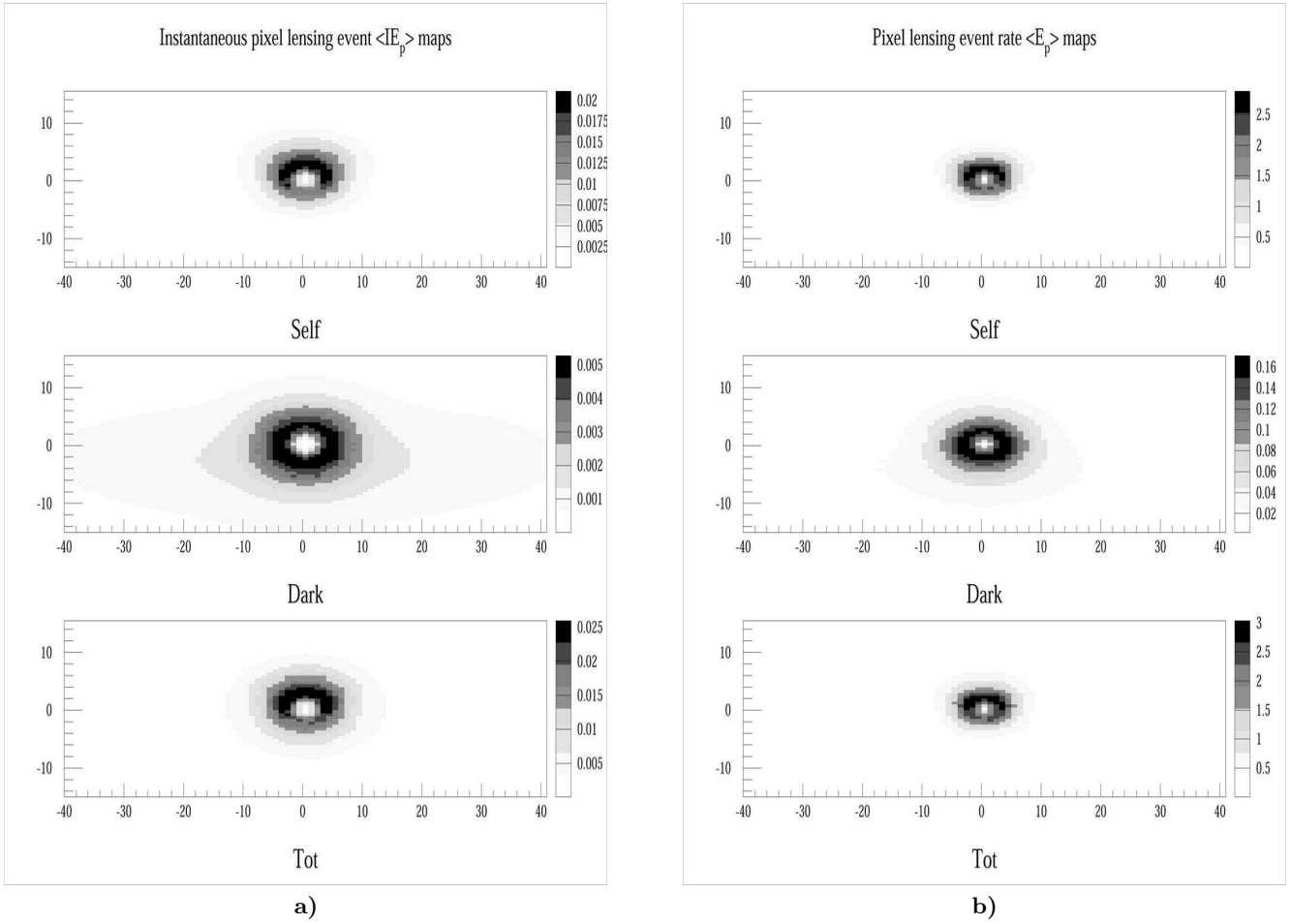


Fig. 5. In panel a), the instantaneous pixel lensing event number density $\langle IE_p(x, y) \rangle$ maps (events per arcmin²) towards M31 are given for self, dark and total lensing. In panel b) maps of pixel lensing event rate $\langle E_p(x, y) \rangle$ (events per year and per arcmin²) are given, in the same cases.

is a geometrical quantity and depends on a small number of parameters and can be used as in eq. (26) to determine the lens nature.

Physically the optical depth is the number of ongoing microlensing events per source star at any instant in time. So, one can also compute the instantaneous event number density, as a function of position, by multiplying the optical depth by the number density of sources

$$\langle IE_c(x, y) \rangle = \langle \tau_c(x, y) \rangle_{n_s} N_s(x, y) \langle f_{RG} \rangle. \quad (28)$$

However, eq. (27) is the usual definition for the optical depth in classical gravitational microlensing, while in the case of pixel lensing it is necessary to take into account the effect of $u_T(M; x, y)$.

In order to generalize the τ definition to the pixel lensing case, a new definition (which joins the advantage of using a geometrical quantity with the main characteristic of the pixel lensing technique, i.e. the effect of the baseline) is introduced (see also Kerins (2004))

$$\langle \tau_p(x, y) \rangle = \langle u_T^2(x, y) \rangle_\phi \langle \tau_c(x, y) \rangle_{n_s}, \quad (29)$$

where $\langle \tau_c(x, y) \rangle_{n_s}$ is

$$\langle \tau_c(x, y) \rangle_{n_s} = \frac{\int \tau_c(x, y) n_s(D_s; x, y) dD_s}{\int n_s(D_s; x, y) dD_s}. \quad (30)$$

The factor $\langle u_T^2(x, y) \rangle_\phi$ in eq. (29) comes from the consideration that the Einstein radius R_E , which enters quadratically in τ_c , has to be multiplied by u_T (always less than unity for pixel lensing).

Accordingly, the instantaneous event number density in pixel lensing is given by

$$\langle IE_p(x, y) \rangle = \langle \tau_p(x, y) \rangle_{n_s} N_s(x, y) \langle f_{RG} \rangle. \quad (31)$$

Here we note that in evaluating $\langle E_p(x, y) \rangle$ for each model considered in Table 1, we have to take into account that the number of detectable pixel lensing events does not depend on **the typical source luminosity** L_s to first order (Kerins, 2004). Indeed, although for a fixed source luminosity L_s the number of sources $N_s \propto L_s^{-1}$, the pixel lensing rate per source $\Gamma_p \propto L_s$,² so that the event num-

² Indeed, the faintest detectable pixel lensing events require a threshold source magnification $A_T \propto L_s^{-1}$, to be seen against

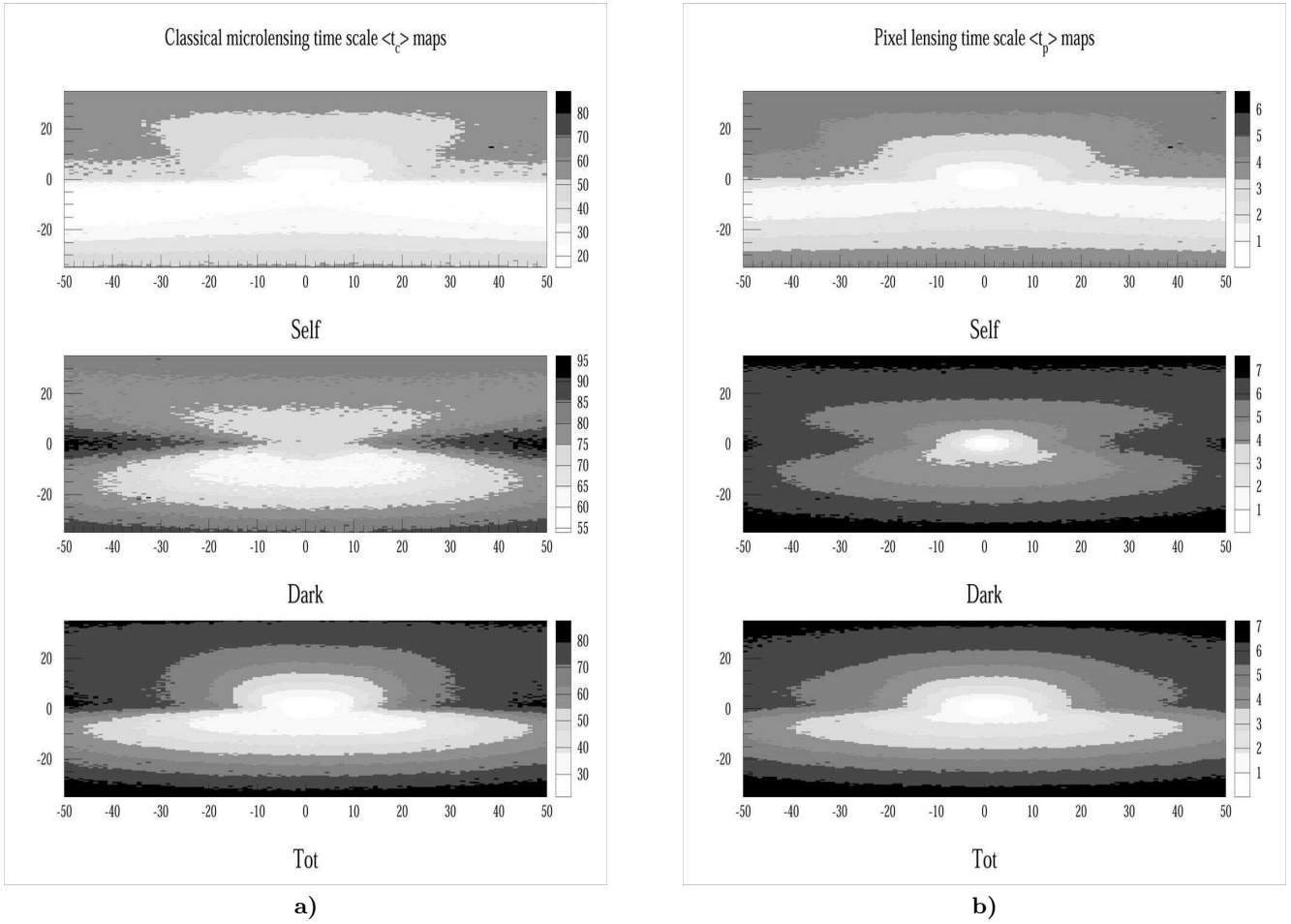


Fig. 6. In panel a), mean classical event duration time $\langle t_c(x, y) \rangle$ (in days) maps towards M31 are given for self, dark and total lensing. In panel b) for pixel lensing, maps of $\langle t_p(x, y) \rangle$ are given, in the same cases.

ber does not depend on L_s . The same also holds for the instantaneous event number density $\langle IE_p(x, y) \rangle$.

5. Pixel lensing event duration

In pixel microlensing, due to the large number of stars simultaneously contributing to the same pixel, the flux from a single star in the absence of lensing is generally not observable. Thus, the Einstein time t_E cannot be determined reliably by fitting the observed light curve.

Indeed, another estimator of the event time duration has been proposed, namely the full-width half-maximum event duration t_{FWHM} , which depends on t_E and u_0 (Gondolo, 1999)

$$t_{FWHM} = t_E w(u_0), \quad (32)$$

where $w(u_0)$ is given by

$$w(u_0) = 2\sqrt{2f[f(u_0^2)] - u_0^2} \quad (33)$$

the local background. On the other hand, in pixel lensing the bulk of observed events involves highly magnified sources for which $A_T \propto u_T^{-1}$. Therefore since $\Gamma_p \propto u_T$, it follows that $\Gamma_p \propto L_s$.

and $f(x) = A(x) - 1$, where $A(x)$ is the amplification factor in eq. (8).

This quantity can be put in a different form (Kerins et al., 2001)

$$t_{FWHM} = 2\sqrt{2}t_E \left(\frac{a+2}{\sqrt{a^2+4a}} - \frac{a+1}{\sqrt{a^2+2a}} \right)^{1/2}, \quad (34)$$

where $a = A_{\max} - 1$.

In the limit of large amplification $A_{\max} \gg 1$ (or, equivalently, $u_0 \ll 1$) one obtains

$$a \simeq \frac{3u_0}{8} + \frac{1}{u_0} - 1 + O(u_0^3). \quad (35)$$

Using eq. (35) in eq. (34), the full-width half-maximum event duration can be approximated by

$$t_{FWHM} \simeq 2\sqrt{2} t_E u_0 (1 - u_0) + O(u_0^3). \quad (36)$$

Clearly, while in classical microlensing u_0 may be determined, in pixel microlensing the background overcomes the source baseline making u_0 unknown, implying that an average procedure on u_0 is needed to estimate the mean event duration. Since the impact parameter u_0 varies in

the range $(0, u_T)$ and the probability of u_0 being in the range $u_0 - u_0 + du_0$ is $P(u_0)du_0 \propto 2\pi u_0 du_0$ (the area of the circular ring of radius u_0 and thickness du_0), by averaging t_{FWHM} on the impact parameter, in the limit of large amplification, one gets

$$\langle t_{FWHM} \rangle_{u_0} \simeq 2\sqrt{2} t_E \frac{\int_0^{u_T} u_0^2 (1 - u_0) du_0}{\int_0^{u_T} u_0 du_0} \simeq u_T t_c, \quad (37)$$

where

$$t_c = \frac{4\sqrt{2}}{3} t_E(x, y). \quad (38)$$

Inspection of the relation in eq. (37) and of eqs. (14), (19) and (29), lead us to introduce for pixel lensing a new event time scale estimator $\langle t_p(x, y) \rangle$ defined as

$$\langle t_p(x, y) \rangle = \langle u_T(x, y) \rangle_\phi \langle t_c(x, y) \rangle_{n_s}, \quad (39)$$

where

$$\langle t_c(x, y) \rangle_{n_s} = \frac{\int t_c(x, y) n_s(D_s; x, y) dD_s}{\int n_s(D_s; x, y) dD_s}, \quad (40)$$

and

$$t_c(x, y) = \frac{4\sqrt{2}}{3} \frac{\int t_E(x, y) d\Gamma(x, y)}{\Gamma(x, y)}. \quad (41)$$

Clearly, the pixel lensing time scale $\langle t_p(x, y) \rangle$ turns out to be the full-width half-maximum event duration averaged over the impact parameter.

6. Results

Before discussing the results obtained, we summarize some assumptions used in the present analysis. First, we assume perfect sensitivity to pixel lensing event detection in M31 pixel lensing searches. Moreover, as reference values, we use the parameters for the Isaac Newton Telescope and WFC (Wide-Field Camera) adopted by the POINT-AGAPE collaboration (Kerins et al., 2001, 2003).

The Telescope diameter, the pixel field of view and the image exposition time are 2.5 m, 0.33 arcsec and $t_{exp} = 760$ s, respectively. We also assume a gain or conversion factor of $2.8 e^-/ADU$, and a loss factor $\simeq 3$, both for atmospheric and instrumental effects. The zero-point with the Sloan-r WFC is ~ 24.3 mag arcsec $^{-2}$.

To take into account the effect of seeing, we employ an analysis based on superpixel photometry. Adopting a value of 2.4 arcsec for the worst seeing value, we take a superpixel dimension of 7×7 pixel and adopt a minimum noise level of $\sigma_T \sim 2.5 \times 10^{-3} N_{bl}$. We also assume that typically 87 per cent of a point spread function (PSF) positioned at the center of a superpixel is contained within the superpixel itself.

The considered sky background is $m_{sky} \simeq 20.9$ mag arcsec $^{-2}$ (corresponding to a Moon eclipse), so that the typical sky luminosity is $N_{sky} \sim 1600$ counts/pixel, which enters in the baseline count estimates. However, for comparison purposes with Kerins (2004), some results in

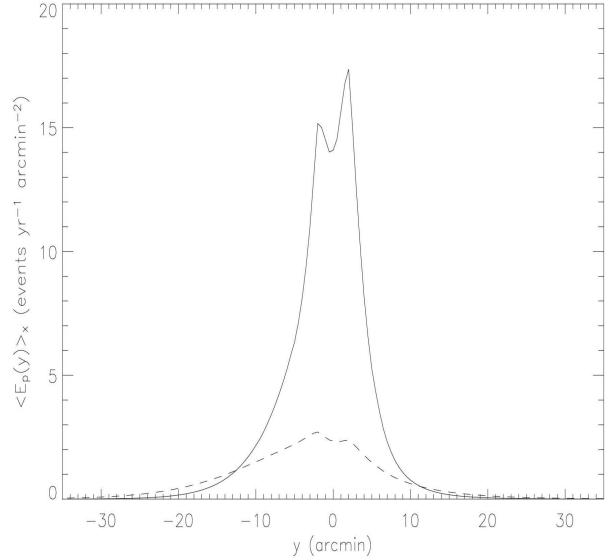


Fig. 7. The projected (along the x axis) mean event number $\langle E_p(y) \rangle_x$ is given as a function of the coordinate y for the Reference model. The dashed line refers to dark lensing events by MACHOs in M31 and MW halos while the solid line is for self-lensing events by stars in M31 bulge and disk.

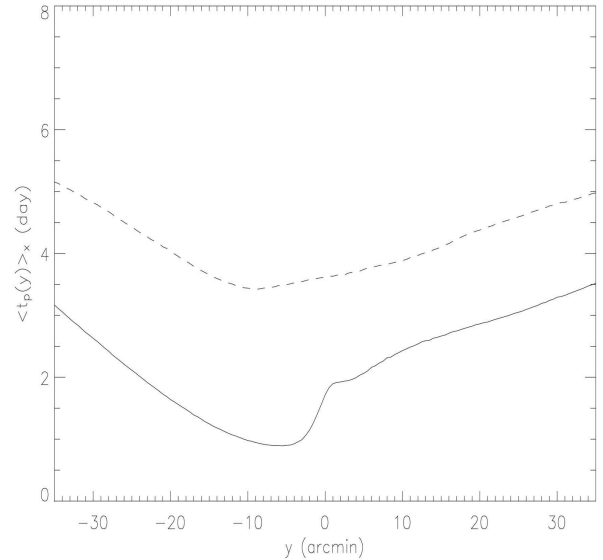


Fig. 8. The pixel lensing event duration $\langle t_p(y) \rangle_x$ averaged along the x direction is given as a function of the y coordinate. The dashed line refers to dark lensing events by MACHOs in M31 and MW halos while the solid line is for self-lensing events by stars in M31 bulge and disk.

Tables 3, 4 and 5 are also given for a sky background $m_{sky} \simeq 19.5$ mag arcsec $^{-2}$ and $f_{see} = 0.40$ (corresponding to a randomly positioned PSF within the superpixel).

Moreover, all the figures presented in Section 6 are given for the Reference model (see Table 1). The effect of varying the model parameters for the M31 bulge, disk and halo is also shown in Tables 3-5.

Finally, we recall that $N_{\text{bl}}(x, y)$ is obtained from eq. (6) where $N_{\text{gal}}(x, y)$ follows from the M31 photometry given by Kent (1989).

6.1. Threshold impact parameter

In Fig. 1 maps of the mean threshold impact parameter $\langle u_T(x, y) \rangle_\phi$ and $\langle u_T^2(x, y) \rangle_\phi$ towards M31 are shown.

In this and following figures we use Cartesian coordinates x and y centered on M31 and aligned along the major and minor axes of the projected light profile, respectively.

As one can see in Fig. 1, the effect of the higher luminosity of the inner region of M31 with respect to the outer part of the galaxy is to reduce the obtained $\langle u_T(x, y) \rangle_\phi$ values by about an order of magnitude.

In Fig. 2, for selected lines of sight to M31, we show how $\langle u_T(x, y) \rangle_\phi$ depends on the photon counts N_{sky} from the background, which is approximated as a diffuse source of magnitude m_{sky} in the range 20.9 – 18.9 mag arcsec⁻². In Fig. 2 we consider several lines of sight to M31 with different (x, y) coordinates (in units of arcmin) in the orthogonal plane. Red lines, from the bottom to the top, refer to (0, -0.2), (4, -0.2) and (8, -0.2), blue lines are for (0, -2), (4, -2) and (8, -2) coordinates. It is evident that $\langle u_T(x, y) \rangle_\phi$ weakly depends on N_{sky} in the inner M31 regions, where N_{bl} is dominated by the counts N_{gal} from the M31 surface brightness. Moreover, for a fixed number of counts N_{sky} from the sky, $\langle u_T(x, y) \rangle_\phi$ decreases with increasing N_{gal} .

We note that by averaging $\langle u_T(x, y) \rangle_\phi$ and $\langle u_T^2(x, y) \rangle_\phi$ (weighting with the star number density) on the whole field of view towards the M31 galaxy, we obtain $\langle u_T \rangle_\phi \simeq 5.10 \times 10^{-2}$ and $\langle u_T^2 \rangle_\phi \simeq 8.8 \times 10^{-3}$.

In Table 2 the effect on $\langle u_T(x, y) \rangle_\phi$ and $\langle u_T^2(x, y) \rangle_\phi$ of changing the parameter values for the superpixel dimension $N \times N$, m_{sky} , f_{see} and σ_T is shown. This is relevant since, referring to the subsequent Tables 3-5, one can verify that the results for the Reference model (in the last two rows) scale with $\langle u_T \rangle_\phi$ (in Tables 3 and 4) and $\langle u_T^2 \rangle_\phi$ (last four rows in Table 5). Therefore, since $\langle u_T(x, y) \rangle_\phi$ and $\langle u_T^2(x, y) \rangle_\phi$ strongly depend on the above mentioned parameters, we expect that all pixel lensing estimated quantities heavily depend on the observing conditions and telescope capabilities.

6.2. Pixel lensing optical depth

Classical microlensing optical depth maps for selected M31 source and lens populations are shown in Fig. 3 for the Reference model.

Here and below, sources and lenses in the M31 bulge and disk are indicated by indices 1 and 2, while lenses in the M31 halo and MW disk and halo by indices 3, 5 and 6. The first and second indices refer to source and lens, respectively.

As one can see, $\langle \tau_c(x, y) \rangle$ always increases towards the M31 center. The well-known far-to-near side asymmetry of the M31 disk is clearly demonstrated in $\langle \tau_c(x, y) \rangle_{23}$, where the lenses are in the M31 halo. Moreover, a strong asymmetry in the opposite direction in the bulge-disk (12) and disk-bulge (21) events (due to the relative source-lens location) is also evident.

We have also found that the classical mean optical depth $\langle \tau_c(x, y) \rangle$ for lenses in our Galaxy ($\langle \tau_c(x, y) \rangle_{15}$, $\langle \tau_c(x, y) \rangle_{25}$, $\langle \tau_c(x, y) \rangle_{16}$ and $\langle \tau_c(x, y) \rangle_{26}$) is almost constant in any direction and therefore we do not show the corresponding maps. For reference, the obtained values are $\langle \tau_c \rangle_{15} \simeq \langle \tau_c \rangle_{25} \simeq 0.03 \times 10^{-6}$ and $\langle \tau_c \rangle_{16} \simeq \langle \tau_c \rangle_{26} \simeq 0.23 \times 10^{-6}$.

In Fig. 4a classical optical depth maps towards M31 are given for self-lensing ($\tau_{\text{self}} = \tau_{11} + \tau_{12} + \tau_{21} + \tau_{22}$) and dark-lensing ($\tau_{\text{dark}} = \tau_{13} + \tau_{16} + \tau_{23} + \tau_{26}$). The total contribution $\tau_{\text{tot}} = \tau_{\text{self}} + \tau_{\text{dark}}$ is given at the bottom of the same figure.

We notice that, in order to evaluate τ_{self} and τ_{dark} , we sum optical depths obtained for different source populations and therefore the averaging procedure in eq. (30) is done by normalizing with the factor $\int [n_1(D_s; x, y) + n_2(D_s; x, y)] dD_s$. Mean pixel lensing optical depth $\langle \tau_p(x, y) \rangle$ maps are shown in Fig. 4b.

As we can see, the main effect of the threshold impact parameter is to substantially decrease $\langle \tau_p(x, y) \rangle$ (with respect to $\langle \tau_c(x, y) \rangle$ values) in particular towards the central regions of M31, as a consequence of the increasing luminosity. Indeed, on average $\langle \tau_p \rangle \simeq \langle u_T^2 \rangle_\phi \langle \tau_c \rangle$ and $\langle u_T^2 \rangle_\phi \simeq 10^{-2}$ (see the third row in Table 2) for the parameter values used in the Figures.

6.3. Pixel lensing rate and expected event number

Maps of the expected number of events in pixel lensing surveys towards M31 are shown in Fig. 5 for the Reference model. As for the optical depth, we give the number of events separately for self-lensing, dark-lensing and also the total contribution.

In Figs. 5a and 5b we show, as a function of position, maps of the instantaneous event number density $\langle IE_p(x, y) \rangle$ (events per arcmin²) and the event rate $\langle E_p(x, y) \rangle$ (events per year and arcmin²).

or the optical depth, the effect of the threshold impact parameter is to produce a decrease of the event number density towards the M31 center (for $r \lesssim 2$ arcmin) and an overall reduction of the event number density with respect to the expectations from classical microlensing results. Moreover, in the figures it is also evident that the inner region (within about 10 arcmin from the M31 center) is dominated by self-lensing events.

In Fig. 7 the projected (along the x axis) mean event number density $\langle E_p(y) \rangle$ as a function of the coordinate y is given. The dashed line refers to dark lensing events by MACHOs in M31 and MW halos while the solid line is for self-lensing events by stars in M31 bulge and disk. The

Table 2. The threshold impact parameters $\langle u_T \rangle_\phi$ and $\langle u_T^2 \rangle_\phi$ averaged over the whole M31 galaxy are given for different values of the superpixel dimension $N \times N$, sky background m_{sky} , fraction f_{see} of the superpixel covered by the PSF and superpixel flux stability σ_T .

$N \times N$	m_{sky} (mag arcsec $^{-2}$)	f_{see}	σ_T	$\langle u_T \rangle_\phi$	$\langle u_T^2 \rangle_\phi$
3 x 3	20.9	0.87	2.5×10^{-3} N _{bl}	1.10×10^{-1}	3.17×10^{-2}
5 x 5	20.9	0.87	2.5×10^{-3} N _{bl}	7.11×10^{-2}	1.59×10^{-2}
7 x 7	20.9	0.87	2.5×10^{-3} N _{bl}	5.10×10^{-2}	9.56×10^{-3}
7 x 7	20.9	0.40	2.5×10^{-3} N _{bl}	2.57×10^{-2}	3.13×10^{-3}
7 x 7	19.5	0.40	2.5×10^{-3} N _{bl}	1.44×10^{-2}	1.17×10^{-3}
7 x 7	19.5	0.40	1.0×10^{-2} N _{bl}	3.82×10^{-3}	1.23×10^{-4}

Table 3. The expected number of events $\langle E_p \rangle$ per year in pixel lensing observations towards the M31 galaxy for different locations of sources and lenses is shown. We consider the 100x70 arcmin 2 region oriented along the major axis of M31, and exclude events occurring within a radius of 8 arcmin of the M31 center. Sources and lenses in the M31 bulge and disk are indicated by indices 1 and 2, while lenses in the M31 halo and MW disk and halo by indices 3, 5 and 6. The first and second indices refer to source and lens, respectively. The mean mass of bulge and disk stars is $\sim 0.31 M_\odot$ and $\sim 0.53 M_\odot$, respectively. For the lenses in the M31 and MW halos we take a mass of $\simeq 0.5 M_\odot$ and a MACHO fraction $f_{\text{MACHO}} \simeq 20\%$.

Model	$\langle u_T \rangle_\phi$	11	12	13	15	16	21	22	23	25	26	overall
Massive halo	5.10×10^{-2}	11.9	16.0	10.7	0.8	4.2	15.9	11.7	25.4	1.7	9.3	107.5
Massive bulge		57.9	100.9	10.4	1.6	9.0	20.8	20.5	8.4	1.1	5.9	236.4
Massive disk		11.8	92.8	3.7	0.7	4.2	16.1	69.3	10.2	1.7	9.4	219.9
Reference		12.5	26.4	8.9	0.8	4.4	13.4	16.0	19.5	1.5	8.3	111.8
Reference	1.4×10^{-2}	3.5	7.2	2.4	0.2	1.2	3.6	4.3	5.2	0.4	2.2	30.4

Table 4. The same as in Table 3 for lenses located in the M31 galaxy. In the last three columns we give the calculated pixel event number for the South/North Semisphere and in brackets their ratio.

Model	$\langle u_T \rangle_\phi$	bulge	disk	M31halo	M31overall	stellar	M31halo	23
Massive halo	5.10×10^{-2}	27.7	27.7	36.1	91.5	31.4/24.0(1.3)	25.3/10.8(2.3)	19.6/5.8(3.4)
Massive bulge		78.6	121.4	18.7	218.7	72.6/127.4(0.6)	11.3/7.4(1.5)	6.0/2.4(2.5)
Massive disk		27.9	162.0	13.9	203.8	85.5/104.5(0.8)	9.2/4.7(1.9)	7.2/2.9(2.5)
Reference		25.9	42.4	28.4	96.7	33.9/34.4(1.0)	19.6/8.9(2.2)	14.9/4.6(3.2)
Reference	1.4×10^{-2}	7.1	11.5	7.7	26.3	9.3/9.4(1.0)	5.3/2.4(2.2)	4.0/1.2(3.2)

North/South asymmetry is evident for dark events that are relatively more numerous in the South Semisphere, corresponding to the far side of the M31 disk.

In Table 3, for selected locations of sources (stars in M31 bulge and disk) and lenses (stars in M31 bulge and disk, stars in MW disk and MACHOs in M31 and MW halos) we give the expected total number of events detectable by monitoring for 1 year the 100x70 arcmin 2 region oriented along the major axis of M31 (events within 8 arcmin from the center are excluded). The first four lines refer to the models considered in Table 1 and to the parameters in the third row of Table 2. As one can see, the obtained results for the Reference model are intermediate with respect to those for the other more extreme models.

In the last row of Table 3, for the Reference model we show how the expected event number changes considering a different value of $\langle u_T \rangle_\phi \simeq 1.44 \times 10^{-2}$ (see 5th row in

Table 2). As expected, one can verify that roughly the event number scales as $\langle u_T \rangle_\phi$.

Similar results have been obtained in previous simulations (see, e.g. Kerins (2004) and references therein). We also note that our numerical results scale with the fraction of halo dark matter in form of MACHOs and with the MACHO mass by a factor $(f_{\text{MACHO}}/0.2) \sqrt{0.5 M_\odot/m_l}$.

In Table 4 we give the total event number $\langle E_p \rangle$ for different lens populations (bulge, disk and halo) located in M31. As one can see, the ratio dark/total events depends on the considered model, varying from 0.07 (for the massive disk model) to 0.40 for the massive halo model.

To study the far-disk/near-disk asymmetry, in the last three columns of Table 4 we give results for the South/North M31 Semispheres and in brackets their ratio. For the Reference model, we find that self-lensing events are roughly symmetric (the same is true for lenses located in the MW disk and halo, not given in the table), while

events due to lenses in M31 halo are asymmetrically distributed with a ratio of about 2. The asymmetry is particularly evident (in the last column of the table) for sources located in the disk.

In Table 5 the instantaneous total number of events $\langle IE_p \rangle$ within the considered M31 region is given. The first four rows refer to the parameter values $\langle m_b \rangle \simeq 0.31 M_\odot$, $\langle m_d \rangle \simeq 0.53 M_\odot$, $f_{MACHO} = 0.2$ and $\langle u_T^2 \rangle_\phi \simeq 9.56 \times 10^{-3}$ (used throughout the paper). For comparison with the results obtained by Kerins (2004), in the last four rows of Table 5 we present our results for $\langle m_b \rangle \simeq 0.5 M_\odot$, $\langle m_d \rangle \simeq 0.5 M_\odot$, $f_{MACHO} = 1$ and $\langle u_T^2 \rangle_\phi \simeq 1.17 \times 10^{-3}$. The asymmetry ratio we obtain is always rather smaller than that quoted by Kerins (2004).

As it has been mentioned by several authors, in order to discriminate between self and dark lensing events, it is important to analyze the event duration. Indeed self-lensing events are expected to have, on average, shorter duration with respect to events due to halo MACHOs.

6.4. Pixel lensing event time scale

Maps of mean event duration time scale in classical and pixel lensing are shown in Fig. 6a and 6b.

Here we use the probability, for each location of sources and lenses given in eq. (26), of obtaining event duration maps for self and dark microlensing events.

As expected, short duration events are mainly distributed towards the inner regions of the galaxy and this occurs for both $\langle t_c(x, y) \rangle$ and $\langle t_p(x, y) \rangle$. The main effect of $\langle u_T(x, y) \rangle_\phi$ is to decrease the event time scale, in particular towards the inner regions of M31, giving a larger number of short duration events with respect to expectations based on $\langle t_c(x, y) \rangle$ calculations.

Both for self and dark events the pixel lensing time scale we obtain is $\simeq 1 - 7$ days, in agreement with results in Kerins (2004), but much shorter with respect to the duration of the events observed by the MEGA Collaboration (de Jong et al., 2004). This is most likely due to the fact that current experiments may not detect events shorter than a few days.

However, the pixel lensing time scale values depend on $\langle u_T(x, y) \rangle_\phi$ and ultimately on the observational conditions and the adopted analysis procedure. Indeed from Table 2 one can see that the $\langle u_T(x, y) \rangle_\phi$ value may be easily doubled, changing the adopted parameters and therefore giving longer events.

In Fig. 8 the pixel lensing event duration $\langle t_p(y) \rangle$ averaged along the x direction is given as a function of the y coordinate. The dashed line refers to dark lensing events by MACHOs in M31 and MW halos while the solid line is for self-lensing events by stars in M31 bulge and disk.

It is clearly evident that dark events last roughly twice as long as self-lensing events and that the shortest events are expected to occur towards the M31 South Semisphere.

The presence of a large number of short duration events in pixel lensing experiments towards M31 has been

reported by several authors (Paulin-Henriksson et al., 2003; Paulin-Henriksson, 2004).

7. Conclusions

We have studied the optical depth, event number and time scale distributions in pixel lensing surveys towards M31 by addressing, in particular, the changes with respect to expectations from classical microlensing (in which the sources are resolved).

Assuming, as reference values, the capabilities of the Isaac Newton Telescope in La Palma and typical CCD camera parameters, exposure time and background photon counts, we perform an analysis consisting of averaging all relevant microlensing quantities over the threshold value $u_T(x, y)$ of the impact parameter. Clearly, as in classical microlensing estimates, an average procedure is also done with respect to all the other parameters entering in microlensing observables: source and lens position, lens mass and source and lens transverse velocities.

The M31 bulge, disk and halo mass distributions are described following the Reference model in Kerins (2004), which provides remarkably good fits to the M31 surface brightness and rotation curve profiles. We also take a standard mass distribution model for the MW galaxy, as described in Section 2, and assume that M31 and MW halos contain 20% $0.5 M_\odot$ MACHOs.

We consider red giants as the sources that most likely may be magnified (and detected in the red band) in microlensing surveys. Moreover, given the lack of precise information about the stellar luminosity function in M31, we assume that the same function holds both for the Galaxy and M31 and does not depend on the position. Accordingly, the fraction of red giants (over the total star number) is $\simeq 5.3 \times 10^{-3}$.

Our main results are maps in the sky plane towards M31 of threshold impact parameter $\langle u_T(x, y) \rangle_\phi$, optical depth $\langle \tau_p(x, y) \rangle$, instantaneous event number density $\langle IE_p(x, y) \rangle$ (events per arcmin² of ongoing microlensing events at any instant in time) and event number density $\langle E_p(x, y) \rangle$ (events per yr and arcmin² to be detected in M31 surveys) and time scale $\langle t_p(x, y) \rangle$.

These maps show an overall reduction of the corresponding classical microlensing results and also a distortion of their shapes with respect to other results in the literature.

Figs. 3 and 4 show maps of the mean optical depth (averaged over the source number density) for the different source and lens locations.

In Fig. 5 we give the instantaneous pixel lensing event number density and the event rate for self, dark and total lensing. It clearly appears that the central region of M31 is dominated by self-lensing events due to sources and lenses in M31 itself, while dark events are relatively more numerous in the outer region (see also Fig. 7).

In Tables 3-4, for the M31 mass distribution models considered by Kerins (2004), we give the expected total event number $\langle E_p \rangle$ to be detected by monitoring, for 1

Table 5. The instantaneous number of events in pixel lensing observations towards the M31 galaxy for different locations of sources and lenses is shown (for details see text). Numbers in brackets refer to the South Semisphere of M31. For the MW disk and halo, lenses in the South Semisphere of the MW contribute to roughly one half of the total and so the corresponding event numbers are not given.

Model	$\langle u_T^2 \rangle_\phi$	bulge	disk	M31halo	M31overall	stellar	M31halo	23
Massive halo	9.56×10^{-3}	0.74	0.57	2.25	3.56	0.68/0.63(1.08)	1.52/0.73(2.09)	1.16/0.42(2.74)
Massive bulge		2.22	2.87	1.37	6.45	1.74/3.34(0.52)	0.83/0.54(1.55)	0.41/0.17(2.46)
Massive disk		0.74	3.35	0.98	5.07	1.32/2.77(0.48)	0.64/0.34(1.86)	0.49/0.21(2.29)
Reference		0.70	0.90	1.78	3.37	0.69/0.90(0.77)	1.21/0.57(2.11)	0.89/0.31(2.89)
Massive halo	1.17×10^{-3}	0.08	0.05	1.34	1.47	0.09/0.05(1.84)	0.95/0.39(2.47)	0.85/0.30(2.82)
Massive bulge		0.20	0.20	0.67	1.08	0.18/0.22(0.82)	0.44/0.23(1.88)	0.32/0.13(2.50)
Massive disk		0.09	0.29	0.58	0.96	0.17/0.21(0.81)	0.39/0.19(2.10)	0.35/0.15(2.32)
Reference		0.08	0.07	1.04	1.19	0.09/0.07(1.32)	0.74/0.29(2.52)	0.66/0.22(2.96)

yr, the 100x70 arcmin² region oriented along the major axis of M31 (the inner 8 arcmin region is excluded). We find that the expected dark to total event number ratio is between 7% (for the massive disk model) and 40% (for the massive halo model). The tables also show the well-known far-disk/near-disk asymmetry due to lenses in the M31 halo. Self-lensing events, instead, are distributed more symmetrically between the M31 North and South Semisphere. Similar conclusions are evident from Table 5, where we give the instantaneous number of events, although the asymmetry ratio we obtain is always smaller than the values quoted by Kerins (2004).

Fig. 6) shows a decrease of the event time scale with respect to classical microlensing, particularly towards the inner regions of M31, due to the high brightness of the galaxy. Both for self and dark lensing events, the pixel lensing time scale we obtain is $\simeq 1 - 7$ days, in agreement with results in the literature. Note that the duration of the events observed by the MEGA Collaboration (de Jong et al., 2004) is typically much longer than 7 days, due to the difficulty of detecting short events in current experiments. It is also clear from Fig. 6 that dark events last roughly twice as long as self-lensing events and that the shortest events are expected to occur towards the M31 South Semisphere (see Fig. 8).

However, we emphasize that the pixel lensing results obtained depend on $\langle u_T(x, y) \rangle_\phi$ and $\langle u_T^2(x, y) \rangle_\phi$ values, and ultimately on the observing conditions and telescope capabilities. Indeed, from Table 2, where the values of $\langle u_T \rangle_\phi$ and $\langle u_T^2 \rangle_\phi$ averaged over the whole M31 galaxy are given, one can verify that pixel lensing quantities scaling with $\langle u_T \rangle_\phi$ ($\langle E_p \rangle$ and $\langle t_p \rangle$) may vary by more than one order of magnitude while quantities scaling with $\langle u_T^2 \rangle_\phi$ ($\langle \tau_p \rangle$ and $\langle IE_p \rangle$) may change by two orders of magnitude.

The present analysis can be used to test estimates and Monte-Carlo simulations by other Collaborations and it has also been performed in view of a planned survey towards M31 by the SLOTT-AGAPE Collaboration (Bozza et al., 2000).

Acknowledgements. We acknowledge S. Calchi Novati, Ph. Jetzer and F. Strafella for useful discussions.

References

- Alcock C. et al. , 1993, *Nat.*, 365, 621.
Alcock C. et al. , 2000, *ApJ*, 542, 281.
Ansari R., Auriere M., Baillon P. et al., 1995, in *Proceedings of the XVII Texas Symposium, Annals of the N.Y. Academy of Sciences*, Eds. Bohringer H., Morfill G. E. and Trumper J. E., Vol 759, p. 608.
Ansari R., Auriere M., Baillon P. et al., 1997, *A&A*, 324, 843.
Ansari R., Auriere M., Baillon P. et al., 1999, *A&A*, 344, L49.
An J. H. et al., 2004, *ApJ*, 601, 845.
Aubourg E., Bareyre P., Brehin S. et al. , 1993, *Nat.*, 365, 623.
Auriere M., Baillon P., Bouquet A. et al., 2001, *ApJ*, 553, L137.
Baillon P., Bouquet A., Giraud-Heraud Y., Kaplan J., 1993, *A&A*, 277, 1.
Baltz E. A., Gyuk G., Crofts A. P. S., 2003, *ApJ*, 582, 30.
Bozza V., Calchi Novati S., Capaccioli M. et al., 2000, *Mem. S.A.It.*, 71, 1113.
Calchi Novati S., Iovane G., Marino A. et al., 2002, *A&A*, 381, 845.
Calchi Novati S., Jetzer Ph., Scarpetta G. et al., 2003, *A&A*, 405, 851.
Caon N., Capaccioli M. and D’Onofrio M., 1993, *MNRAS* 265, 1013.
Colley W. N., 1995, *AJ*, 109, 440.
Crofts A. P. S., 1992, *ApJ*, 399, L43.
Crofts A. P. S. and Tomaney A. B., 1996, *ApJ*, 473, L87.
de Jong J. T. A., Kuijken K., Crofts A. P. S. et al., 2004, *A&A*, 417, 461.
De Paolis F., Ingrassio G., Nucita A. et al., 2004, in preparation
Dwek E., Arendt R. G., Hauser M. G. et al., 1995, *ApJ*, 445, 716,
Giudice G. F., Mollerach S. and Roulet E., 1994, *Phys. Rev. D*, 50, 4.
Gondolo P., 1999, *ApJ*, 510, L29.
Gould A., 1994, *ApJ*, 435, 573.
Griest K., 1991, *ApJ*, 366, 412.

- Gyuk G. and Crotts A. P. S., 2000, ApJ, 535, 621.
Han C., Gould A., 1996, ApJ, 473, 230.
Jetzer Ph., 1994, A&A, 286, 426.
Kent S. M., 1989, AJ, 97, 1614.
Kerins E., Carr B., Ewans N.W. et al., 2001, MNRAS, 323, 13.
Kerins E., An J., Ewans N. W. et al., 2003, ApJ, 598, 993.
Kerins E., 2004, MNRAS, 347, 1033.
Mamon G. A. and Soneira R. M., 1982, ApJ, 255, 181.
Paczynski B., 1986, ApJ, 304, 1.
Paulin-Henriksson S., Baillon P., Bouquet A. et al., 2003, A&A, 405, 15.
Paulin-Henriksson S., 2004, talk at Moriond Conference, <http://moriond.in2p3.fr>.
Reitzel D., Guhathakurta P. and Gould A., 1998, AJ, 116, 707.
Riffeser A., Fliri J., Bender R. et al., 2003, ApJ, 599, L17.
Uglesich R. R., Crotts A. P. S., Baltz E. A., 2004 astro-ph 0403248.